The Astronomical Journal, 141:11 (11pp), 2011 January doi:10.1088/0004-6256/141/1/11
© 2011. The American Astronomical Society. All rights reserved. Printed in the U.S.A.

A *SPITZER* INFRARED SPECTROGRAPH STUDY OF DEBRIS DISKS AROUND PLANET-HOST STARS

Sarah E. Dodson-Robinson[1,5], C. A. Beichman[2], John M. Carpenter[3], and Geoffrey Bryden[4]
[1] Astronomy Department, University of Texas, 1 University Station C1400, Austin, TX 78712, USA; sdr@astro.as.utexas.edu
[2] NASA Exoplanet Science Institute, California Institute of Technology, 770 S. Wilson Ave., Pasadena, CA 91105, USA
[3] Department of Astronomy, California Institute of Technology, Mail Code 249-17, 1200 E. California Blvd., Pasadena, CA 91105, USA
[4] Jet Propulsion Laboratory, California Institute of Technology, 4800 Oak Grove Dr., Pasadena, CA 91109, USA
Received 2010 August 30; accepted 2010 October 15; published 2010 December 7

ABSTRACT

Since giant planets scatter planetesimals within a few tidal radii of their orbits, the locations of existing planetesimal belts indicate regions where giant planet formation failed in bygone protostellar disks. Infrared observations of circumstellar dust produced by colliding planetesimals are therefore powerful probes of the formation histories of known planets. Here we present new *Spitzer* infrared spectrograph (IRS) spectrophotometry of 111 solar-type stars, including 105 planet hosts. Our observations reveal 11 debris disks, including two previously undetected debris disks orbiting HD 108874 and HD 130322. Combining the 32 μm spectrophotometry with previously published MIPS photometry, we find that the majority of debris disks around solar-type stars have temperatures in the range $60 \lesssim T_{\rm dust} \lesssim 100$ K. Assuming a dust temperature $T_{\rm dust} = 70$ K, which is representative of the nine debris disks detected by both IRS and MIPS, debris rings surrounding Sun-like stars orbit between 15 and 240 AU depending on the mean particle size. Our observations imply that the planets detected by radial-velocity searches formed within 240 AU of their parent stars. If any of the debris disks studied here have mostly large, blackbody emitting grains, their companion giant planets must have formed in a narrow region between the ice line and 15 AU.

Key words: circumstellar matter – infrared: stars – Kuiper Belt: general – planetary systems – planets and satellites: formation

Online-only material: color figures

1. INTRODUCTION

Sometimes the giant planets that failed to form reveal as much about the birth environments of other solar systems as the giant planets we actually find. Our objective is to characterize circumstellar dust produced by colliding planetesimals orbiting planet hosts and use the orbital radii of such planetesimals to constrain the locations where the known giant planets may have formed. Radial-velocity searches do not yet have the time baseline to detect giant planets more than ∼7 AU from their host stars. Nevertheless, we expect that giant planets do not reside within observed debris disks—which typically orbit at 10 AU or more—because giant planets scatter planetesimals within a few Roche radii of their orbits (e.g., Bryden et al. 2000; Thommes et al. 2003; Ida & Lin 2004; Goldreich et al. 2004). As long as planetesimal belts do not migrate on a large scale, grain temperature measurements that constrain the location of circumstellar dust highlight the regions in long gone protostellar disks where giant planet formation did not succeed.

The "Vega Phenomenon"—an excess of infrared emission caused by circumstellar dust—was first observed by Aumann et al. (1984) using the *Infrared Astronomical Satellite*. Since then, observations by the *Spitzer Space Telescope* have revealed the temperatures and locations of scores of extrasolar Kuiper Belts (e.g., Chen et al. 2006; Hillenbrand et al. 2008). Here we combine new *Spitzer* infrared spectrograph (IRS) spectrophotometry of planet hosts with previously published MIPS data, allowing us to constrain grain temperatures and planetesimal belt locations and exclude regions inhabited by circumstellar debris from the possible giant planet formation zone.

Massive planets with small orbital radii almost certainly formed at larger radii, where they had access to abundant solid material (Bodenheimer et al. 2000), and migrated inward through either dynamical interactions with massive gas disks (Lin et al. 1996) or Kozai cycles triggered by a companion (Libert & Tsiganis 2009). Migration will disrupt any planetesimal belt in the giant planet's path, increase the collision rate of planetesimals, and accelerate the evolution of the planetesimal belt to reduce the debris production at older ages. Indeed, migration of the gas-giant planets in our own solar system and the subsequent disruption of the Kuiper Belt is one possible explanation for the Late Heavy Bombardment that occurred in the inner solar system 3.9 Gyr ago (Gomes et al. 2005). Raymond et al. (2006) found that if migration occurs quickly and the planet settles at an orbital radius <0.25 AU, the planetesimal disk can regenerate to form terrestrial planets, and consequently may form a long-lived debris disk. However, disk regeneration is suppressed if the migration stops at a radius $a > 0.5$ AU and the debris may dissipate rapidly.

The evidence for brighter debris disks around planet hosts than non-hosts has at times been intriguing (e.g., Beichman et al. 2005; Kóspál et al. 2009), but most studies show no statistically significant differences between the circumstellar dust populations of planet hosts and other stars (Moro-Martín et al. 2007; Bryden et al. 2009)). Despite a few compelling exceptions—for example, the existence and location of Fomalhaut b was predicted through analysis of the shape and surface brightness profile of Fomalhaut's debris disk (Quillen 2006; Kalas et al. 2008)—statistical analysis indicates that known giant planets tend to be dynamically decoupled from any planetesimal belts orbiting their host stars.

Since 60% of the exoplanets discovered at the time of this writing have semimajor axes >0.5 AU,[6] we expect that few planetesimal belts in the path of migrating planets were able to regenerate according to the Raymond et al. (2006)

[5] Former Spitzer Fellow.

[6] Based on histograms provided by the Exoplanet Encyclopedia, http://exoplanet.eu.

scenario. The simplest hypothesis, then, is that migratory planets formed nearer their host stars than the dust-producing planetesimal belts generally studied with *IRAS* and *Spitzer*. Migrating inward, they left the planetesimal belts intact. Since giant planet formation efficiency decreases with distance from the star (Safronov 1969; Pollack et al. 1996), we expect that today's planetesimal belts had too little solid mass to overcome the growth slowdown inherited from their wide orbits. Excepting cases where observations conclusively demonstrate that a particular debris disk and giant planet dynamically interact (Quillen 2006; Lovis et al. 2006; Kalas et al. 2008), the ensemble of debris disks orbiting known radial-velocity planet hosts provides an upper limit to the semimajor axis of the locations where most of the known planets could have formed.

In Section 2, we describe our sample of target stars. In Sections 3 and 4, we detail our procedure for reducing *Spitzer* IRS data and detecting infrared excesses. In Section 5, we discuss our debris disk detections. We focus specifically on the luminosity and location of the dust in Section 6. Finally, we list our conclusions in Section 7.

2. SAMPLE SELECTION AND OBSERVATIONS

The main sample of extrasolar planetary systems was selected for *Spitzer* program 40096 (PI: J. Carpenter) from the compilation reported in the Extrasolar Planets Encyclopaedia (http://exoplanet.eu) as of 2007 February 16. At the time, there were 182 known extrasolar systems containing 212 planets. From this parent sample, we selected extrasolar planetary systems that met the following criteria.

1. The planets were discovered by radial-velocity techniques or from transiting surveys and later confirmed by radial-velocity measurements. We excluded planets identified from microlensing surveys, pulsar timing experiments, and direct imaging of star-forming regions.
2. Target stars had distances available from *Hipparcos* parallaxes.
3. Targets had either main-sequence or sub-dwarf luminosity class to focus the survey on solar analogs.
4. Targets were bright enough to reach a signal-to-noise ratio (S/N) of 20 in a spectrophotometric bandpass between 30 and 34 μm within 20 AOR cycles of 120 s.

These criteria narrowed the list to 143 planet hosts, all within a distance of 100 pc, containing 171 planets. Stellar age estimates for the sample are available from the detailed spectroscopic work by Valenti & Fischer (2005) and/or Ca II H and K stellar activity measurements (Saffe et al. 2005; Wright et al. 2004). We cross-correlated this list of stars with the Reserve Object Catalog using a 5 × 5 arcmin search area and identified 34 extrasolar planet hosts with previous IRS observations, leaving 109 stars for our IRS observing program. We excluded seven stars observed in program 40096 from our final sample because of poor sky subtraction or stray light from nearby sources.

After the observations were complete, the existence of the planet orbiting HD 188753 (Konacki 2005) was challenged by Eggenberger et al. (2007). Here we present our observations of HD 188753 but classify it as a non-host. Information about our sample, including the number of planets orbiting each star and the 70 μm dust luminosity, is given in Table 1. Effective temperatures were taken from the following sources in order of preference: (1) Valenti & Fischer (2005, abbreviated VF05 in Table 1), (2) Santos et al. (2004b), and (3) the planet discovery paper.

We also present observations of nine solar-type stars with previously unpublished data from other IRS programs. From IRS program 41 (PI: G. Rieke), we included the planet hosts HD 50554, HD 52265, HD 117176 (70 Vir), and HD 134987, bringing the total number of planet hosts in our sample to 105. Finally, we included the stars without planets HD 166, HD 33262, and HD 33636 from program 41, and HD 105211 and HD 219482 from program 2343 (PI: C. Beichman). Our final sample includes 111 stars, six of which have no detected planets.

Of the stars in our sample, 109 are FGK dwarfs and two, GJ 876 and GJ 581, are M dwarfs. All but three of the stars have 70 μm photometry either from the MIPS component of our observing campaign, described by Bryden et al. (2009), or from previous surveys. All but six of our targets are older than 1 Gyr, which reduces any spurious statistical effects that might result from the well-known correlation between debris disk brightness and stellar age (Su et al. 2006). Thus, our discovered debris disks contain information about the planetesimal populations of mature planetary systems such as our own.

The Infrared Spectrograph (IRS) aboard the *Spitzer Space Telescope* observed 102 targets from program 40096 between 2007 July and 2008 January (IRS campaigns 42–47). For each star, we recorded five 6 s exposures in the SL1 module to characterize the stellar photosphere between 7 and 14 μm. All stars received a minimum exposure time of 30 s (five 6 s cycles) in the LL2 and LL1 modules, with extra cycles and/or ramp time added as needed for faint targets to detect the photosphere at the 2σ–3σ level in each resolution element. We imposed a maximum integration time of 120 s with 20 cycles to keep the AORs to a reasonable length. We also required a minimum of five cycles to achieve the redundancy needed to identify cosmic rays and bad pixels, and to compute uncertainties based on repeatability of the spectral extraction. The IRS follow-up observations of 70 μm excesses from IRS programs 41 and 2343 went deeper in the LL1 module, reaching S/N $\approx$ 20 per resolution element between 30 and 34 μm.

3. DATA ANALYSIS

Bad pixels were identified using the campaign-specific rogue pixel masks provided by the Spitzer Science Center. We used the IRSCLEAN package to remove bad pixels from the *Spitzer* pipeline's basic calibrated data. Sky subtraction and spectral extraction were performed with the SMART data reduction package developed by the IRS instrument team at Cornell (Higdon et al. 2004). Each star was observed at two positions along the slit, Nod 1 and Nod 2. For each nod, we constructed sky and stray-light correction frames by taking the median of all exposures performed in the same module but opposite nod.

To make the end-to-end spectrum, we clipped unreliable data points from the beginning and end of each order. We retained SL1 data from 7 to 14 μm, LL2 data from 14 to 20 μm, and LL1 data from 20 to 35 μm. We imposed a requirement that the final spectrum be continuous over order crossings to correct for the different slit losses in each order. A smooth spectrum was produced by correcting the LL2 spectrum with a constant scaling factor to match the SL1 flux in the overlap region at 14 μm, then scaling LL1 fluxes to match LL2 in the 20 μm overlap region.

The final step in our data reduction process was to create a model of the star's photosphere. For each FGK star, we used the Atlas9 grid of model atmospheres for stars with solar abundance ratios (Kurucz 1992). Following the recommendations of

Table 1
Observed Stellar Sample

HD	Name	Spectral Type	$T_{\rm eff}$(K)	$T_{\rm eff}$ Reference	V (mag)	Dist. (pc)	Planets	$\frac{L_{\rm dust}}{L_*} \times 10^5$ (70 μm)	70 μm Reference
...	GJ 581	M3	3310	Bessell (1995)	10.57	6.3	3	8.49	Kóspál et al. (2009)
...	GJ 876	M4	3130	Bessell (1995)	10.17	4.7	3	< 3.2	Kóspál et al. (2009)
...	Hip 14810	G5	5485	Wright et al. (2009)	8.52	52.9	3	...	...
142		F7V	6248	VF05[a]	5.70	25.6	1	0.8	B09[b]
166		K0V	5577	VF05	6.13	13.7	0	6.0	Trilling et al. (2008)
1237	GJ 3021	G8.5Vk:	5360	Santos et al. (2004b)	6.59	17.6	1	< 1.0	B09
3651		K0V	5220	VF05	5.80	11.1	1	< 1.1	B09
4203		G5	5701	VF05	8.69	77.8	1	< 23.9	B09
4208		G7VFe-1H-05	5600	VF05	7.79	32.7	1	< 2.9	B09
8574		F8	6049	VF05	7.11	44.2	1	< 1.5	B09
10697	109 Psc	G5IV	5680	VF05	6.29	32.6	1	< 1.3	B09
11964		G5	5349	VF05	6.42	34.0	2	< 1.0	B09
12661		K0V	5742	VF05	7.44	37.2	2	< 6.5	B09
13445	GJ 86	K1V	5150	VF05	6.17	10.9	1	...	...
16141		G5IV	5793	VF05	6.78	35.9	1	< 2.6	B09
17051	HR 810	F9VFe+03	6038	Rocha-Pinto & Maciel (1998)	5.40	17.2	1	< 0.5	B09
19994		F8V	6188	VF05	5.06	22.4	1	0.5	B09
20367		G0	6100	Santos et al. (2004b)	6.41	27.1	1	< 1.1	B09
20782		G1.5V	5758	VF05	7.38	36.0	1	< 2.1	B09
23079		F9.5V	5927	VF05	7.12	34.6	1	< 0.9	B09
23127		G2V	5752	VF05	8.58	89.1	1	< 7.3	B09
23596		F8	5903	VF05	7.25	52.0	1	< 3.1	B09
27442	ϵ Ret	K2III	4845	VF05	4.44	18.2	1	< 0.3	B09
27894		K2V	4875	Santos et al. (2005)	9.42	42.4	1	< 10.6	B09
28185		G6.5IV-V	5656	Santos et al. (2004b)	7.80	39.6	1	< 5.7	B09
30177		G8V	5607	VF05	8.41	54.7	1	< 11.2	B09
33262	ζ Dor	F7V	6200	Flower (1996)	4.72	11.7	0	0.51	Trilling et al. (2008)
33283		G4V	5995	Johnson et al. (2006)	8.05	86.9	1	< 4.9	B09
33564		F6V	6250	Nordström et al. (2004)	5.10	21.0	1	< 0.5	B09
33636		G0VH-03	5904	VF05	7.06	28.7	0	5.1	Trilling et al. (2008)
37124		G4IV-V	5500	VF05	7.68	33.2	3	< 7.2	B09
37605		K0	5475	Cochran et al. (2004)	8.69	42.9	1	< 23.2	B09
40979		F8	6089	VF05	6.73	33.3	1	1.44	Kóspál et al. (2009)
41004	HD 41004 A	K1V	5010	Santos et al. (2002)	8.65	43.0	1	< 6.9	B09
45350		G5	5616	VF05	7.88	48.9	1	< 7.2	B09
46375		K1IV	5285	VF05	7.84	33.4	1	17.8	Kóspál et al. (2009)
49674		G0	5662	VF05	8.10	40.7	1	< 4.5	B09
50499		G1V	6069	VF05	7.21	47.3	1	1.6	Kóspál et al. (2009)
50554		F8V	5928	VF05	6.84	31.0	1	5.85	Trilling et al. (2008)
52265		G0V	6076	VF05	6.30	28.1	1	2.69	Trilling et al. (2008)
63454		K3V	4841	VF05	9.37	35.8	1	< 16.0	B09
65216		G5V	5666	Santos et al. (2003)	7.97	35.6	1	< 4.4	B09
68988		G0	5960	VF05	8.20	58.8	1	< 4.2	B09
70642		G6VCN+05	5705	VF05	7.18	28.8	1	< 6.3	B09
72659		G0	5919	VF05	7.46	51.4	1	< 2.2	B09
73256		G8IV-VFe+05	5570	Udry et al. (2003)	8.08	36.5	1	< 5.5	B09
74156		G0	6067	VF05	7.61	64.6	3	< 3.4	B09
75289		F9VFe+03	6095	VF05	6.36	28.9	1	< 14.9	B09
76700		G6V	5668	VF05	8.13	59.7	1	< 3.7	B09
81040		G0	5700	Sozzetti et al. (2006)	7.72	32.6	1	< 3.2	B09
83443		K0V	5453	VF05	8.24	43.5	1	< 9.0	B09
88133		G5IV	5494	Fischer et al. (2005)	8.06	74.5	1	...	...
89307		G0V	5897	VF05	7.01	30.9	1	< 2.8	B09
89744		F7V	6291	VF05	5.74	39.0	1	< 0.9	B09
93083		K2IV-V	4995	Lovis et al. (2005)	8.33	28.9	1	< 9.2	B09
99492		K2V	4954	VF05	7.57	18.0	1	< 5.1	B09
102117		G6V	5695	VF05	7.47	42.0	1	< 16.8	B09
102195		K0	5291	Melo et al. (2007)	8.06	29.0	1	< 9.2	B09
105211	η Cru	F2V	6600[c]	Peletier (1989)	4.15	19.7	0	6.9	Beichman et al. (2006a)
107148		G5	5797	VF05	8.01	51.3	1	< 5.6	B09
108147		F8VH+04	6156	VF05	7.00	38.6	1	< 23.9	B09
108874		G5	5550	VF05	8.74	68.5	2	< 13.6	B09
109749		G3V	5903	Fischer et al. (2006)	8.08	59.0	1	< 6.2	B09
111232		G8VFe-10	5494	Santos et al. (2004b)	7.61	28.9	1	< 6.1	B09
114386		K3V	4819	VF05	8.73	28.0	1	< 6.8	B09
114762		F9V	5952	VF05	7.30	40.6	1	< 3.3	B09

Table 1
(Continued)

HD	Name	Spectral Type	$T_{\rm eff}$(K)	$T_{\rm eff}$ Reference	V (mag)	Dist. (pc)	Planets	$\frac{L_{\rm dust}}{L_*} \times 10^5$ (70 μm)	70 μm Reference
114783		K0	5135	VF05	7.56	20.4	1	< 3.0	B09
117176	70 Vir	G5V	5544	VF05	5.00	18.1	1	0.97	Trilling et al. (2008)
117207		G7IV-V	5723	VF05	7.26	33.0	1	< 2.1	B09
117618		G0V	5963	VF05	7.17	38.0	1	< 2.3	B09
118203		K0	5695	da Silva et al. (2006)	8.05	88.6	1	< 13.2	B09
130322		K0III	5308	VF05	8.04	29.8	1	< 7.9	B09
134987	23 Lib	G5V	5750	VF05	6.45	25.7	2	< 2.70	Trilling et al. (2008)
136118		F8	6097	VF05	6.93	52.3	1	< 1.3	B09
142415		G1V	5901	VF05	7.34	34.6	1	< 10.9	B09
143761	ρ Cr B	GOV	5823	VF05	5.40	17.4	1	< 0.6	B09
145675	14 Her	K0V	5347	VF05	6.67	18.1	2	< 1.0	B09
147513		G1VH-04	5929	VF05	5.38	12.9	1	< 1.6	B09
149026		G0IV	6147	Sato et al. (2005)	8.15	78.9	1	< 5.2	B09
149143		G0	5884	Fischer et al. (2006)	7.89	63.5	1	< 4.6	B09
154857		G5V	5605	VF05	7.24	68.5	1	< 4.7	B09
159868		G5V	5623	VF05	7.24	52.7	1	< 9.9	B09
160691	μ Arae	G3IV-V	5784	Santos et al. (2004a)	5.15	15.3	4	< 0.9	B09
162020		K2V	4844	VF05	9.10	31.3	1	< 28.6	B09
168443		G6V	5579	VF05	6.92	37.9	2	< 14.7	B09
169830		F7V	6221	VF05	5.91	36.3	2	< 1.5	B09
177830		K0	4948	VF05	7.18	59.0	1	< 1.4	B09
183263		G2IV	5936	VF05	7.86	52.8	2	< 9.1	B09
185269		G0IV	5980	Johnson et al. (2006)	6.68	47.4	1	< 2.4	B09
186427	16 Cyg B	G3V	5674	VF05	6.20	21.4	1	< 1.3	B09
187085		G0V	6075	VF05	7.22	45.0	1	2.3	Kóspál et al. (2009)
187123		G5	5814	VF05	7.83	47.9	2	< 10.6	B09
188015		G5IV	5745	VF05	8.24	52.6	1	< 29.4	B09
188753	HD 188753 A	G8V	5750	Konacki (2005)	7.40	44.8	0[d]	< 8.7	B09
190360		G7IV-V	5551	VF05	5.71	15.9	2	< 9.7	B09
192263		K2V	4975	VF05	7.79	19.9	1	5.4	B09
192699		G5	5220	Johnson et al. (2007)	6.45	67.4	1	< 1.1	B09
195019		G3IV-V	5788	VF05	6.91	37.4	1	< 2.1	B09
196050		G3V	5892	VF05	7.50	46.9	1	< 2.7	B09
196885		F8IV	6185	VF05	6.40	33.0	1	< 1.0	B09
202206		G6V	5787	VF05	8.08	46.3	2	14.3	B09
208487		G2V	6067	VF05	7.47	44.0	1	< 4.9	B09
210277		G0V	5555	VF05	6.63	21.3	1	< 0.8	B09
212301		F8V	6256	Lo Curto et al. (2006)	7.76	52.7	1	< 4.9	B09
213240		G0/G1V	5967	VF05	6.80	40.7	1	< 1.1	B09
216435		G0V	5999	VF05	6.03	33.3	1	2.2	B09
216770		G9VCN+1	5229	Mayor et al. (2004)	8.10	37.9	1	< 19.0	B09
217107		G8IV	5704	VF05	6.18	19.7	2	< 1.5	B09
219482		F6V	6240	Flower (1996)	5.66	20.6	0	2.8	Beichman et al. (2006a)
222404	γ Cep	K1IV	4916	Santos et al. (2004b)	3.23	13.8	1	< 0.3	B09
222582		G5	5726	VF05	7.68	41.9	1	< 2.3	B09
224693		G2V	6037	Butler et al. (2006)	8.23	94.1	1	< 8.0	B09

Notes.
[a] VF05: Valenti & Fischer (2005).
[b] B09: Bryden et al. (2009).
[c] Based on tabulated values for $T_{\rm eff}$ versus $V - K$.
[d] Planet's existence under debate; see Eggenberger et al. (2007b).

Bertone et al. (2004), we used the NextGen model atmospheres (Hauschildt et al. 1999) for photospheres of the M dwarfs GJ 876 and GJ 3021, which have effective temperatures less than 4000 K.

Photosphere models were fitted using *Hipparcos* parallaxes and *Hipparcos*/*Tycho* BT and VT magnitudes (Perryman et al. 1997; Høg et al. 2000) transformed to the Johnson photometric system, Two Micron All Sky Survey (2MASS) J, H, and Ks magnitudes (Cutri et al. 2003), and the measured temperature of each star from planet-search spectra. Sources of $T_{\rm eff}$ measurements are listed in Table 1. When available, R and I photometry from Bessell (1990) with assumed 0.1 mag uncertainties were added to further constrain the photosphere models. Each model photosphere was extrapolated to mid-infrared wavelengths using a simple blackbody extension to the optical and near-infrared fit.

In the next section, we describe our method for detecting non-photospheric emission, the signature of circumstellar dust.

4. DETECTING EXCESS EMISSION

To construct the infrared excess spectra, we subtracted the model photosphere from the IRS spectrum of each star and

calculated the fractional flux in each resolution element relative to the photosphere:

$$f_\nu = \frac{F_\nu(\text{observed}) - F_\nu(\text{photosphere})}{F_\nu(\text{photosphere})}. \quad (1)$$

Spitzer MIPS 24 μm observations of a sample of FGK dwarfs with median age 4 Gyr have demonstrated that only $\sim$1% of main-sequence solar-type stars have dust with luminosity $L_{\rm dust}/L_* > 10^{-5}$ at 24 μm (Bryden et al. 2006), which originates from asteroid-belt analogs at 3–4 AU from Sun-like host stars. The fractional excess spectrum of a solar-type star with a typical debris disk should stay near zero until between 25 and 30 μm, at which point the dust gives it a rising slope. With the low likelihood of detecting short-wavelength excesses in mind, our first step in calculating the fractional excess spectrum was to assume the first 10 resolution elements (20.93–22.45 μm) of our clipped LL1 spectra defined the photosphere, such that

$$\frac{1}{\Delta\nu}\int_{20.93\,\mu\text{m}}^{22.45\,\mu\text{m}} f_\nu d\nu = 0, \quad (2)$$

where $\Delta\nu$ is the frequency interval between 20.93 and 22.45 μm.

In the previous section, we described using the order overlap regions to correct for differential slit losses, a procedure that produces a smooth but not flux-calibrated spectrum. In order to perform spectrophotometry of our sources it is essential that we avoid the unreliable parts of our spectra—the well-known SL1 order curvature and the LL1 24 μm flux deficit.[7] Pinning the short-wavelength end of LL1 to the photosphere model defines a flux calibration using an instrumentally reliable part of our spectra that should contain only photospheric emission. In two cases, where we did observe a rising fractional excess slope shortward of the 20.93 μm LL1 boundary (HD 166 and HD 219482), we used the first 10 resolution elements of LL2 (14.24–15.00 μm) to define the photosphere.

Following the approach of Beichman et al. (2006b) and Lawler et al. (2009), we defined a filter spanning 30–34 μm which is primarily sensitive to dust with $T \approx 115$ K. Such dust would be located between 8 and 10 AU from a Sun-like star assuming blackbody grains. To search for debris disks, we calculate the frequency-weighted mean excess relative to the photosphere in the 30–34 μm filter. The excess measurement error σ based on uncertainties propagated through the *Spitzer* pipeline and photospheric fitting error is

$$\sigma^2 = \frac{1}{\Delta\nu}\int_{30\,\mu\text{m}}^{34\,\mu\text{m}} \sigma_{\nu,\text{obs}}^2 d\nu + (0.02\,F_*)^2. \quad (3)$$

In Equation (3), $\sigma_{\nu,\text{obs}}$ is the uncertainty in each resolution element from the *Spitzer* pipeline propagated through the SMART data reduction, ν is the frequency of each resolution element, and $\Delta\nu$ is the frequency difference between 30 and 34 μm. The star flux F_* in Equation (3) is simply the frequency-weighted average flux of the photosphere model between 30 and 34 μm:

$$F_* = \frac{1}{\Delta\nu}\int_{30\,\mu\text{m}}^{34\,\mu\text{m}} F_\nu(\text{photosphere}) d\nu. \quad (4)$$

Following Beichman et al. (2006b), we impose a minimum fractional photosphere fitting uncertainty of 2%, which gives the $(0.02\,F_*)^2$ component of the variance. In writing Equation (3) we assume that the observational errors in each resolution element are independent.

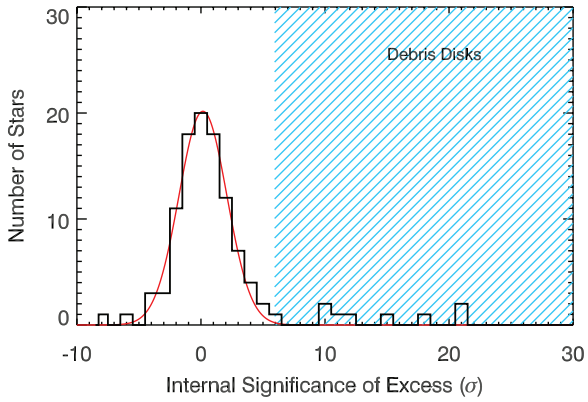

Figure 1. Debris disks were identified by fitting a Gaussian distribution, plotted in red, to a histogram of fractional 30–34 μm excesses. The histogram variable, shown in black, is the number of standard deviations σ of the measured excess from a perfect photosphere, where σ is the frequency-weighted quadrature sum of the internal measurement error and photosphere fitting error. Our sample has an overall fractional excess dispersion of $\Sigma = 1.93\sigma$ (see Equation (5)). The blue cross-hatched region contains our debris disks, which have fractional infrared excesses greater than 3Σ. Our sample includes 11 stars with statistically significant 30–34 μm excesses.

(A color version of this figure is available in the online journal.)

If the errors reported by the *Spitzer* pipeline/SMART and the 2% photosphere-fitting uncertainty account for all of the dispersion in our infrared excess measurements, we expect only one source to have more than a 2σ flux deficit. However, a closer look at the distribution of excesses in our sample reveals seven stars with 2σ–3σ flux deficits between 30 and 34 μm, indicating that there is an extra source of error in our infrared excess measurements. Before conclusively identifying any debris disks, we follow Beichman et al. (2006b) and require that they have a significant infrared excess relative to the dispersion of the entire sample, not just internal measurement and fitting errors. Accordingly, we rank each debris disk candidate by the significance of its infrared excess against the internal error σ. With such a ranking system we can identify low-luminosity debris disks in high signal-to-noise observations while rejecting debris disk candidates that appear to be bright but also have large measurement errors.

We construct a histogram in the variable

$$N = \frac{F_{\text{obs}} - F_*}{\sigma}, \quad (5)$$

where N is the number of standard deviations σ from a perfect photosphere in the 30–34 μm filter and F_{obs} is the frequency-weighted average observed flux. We can calculate F_{obs} by replacing the predicted photospheric flux F_ν(photosphere) in Equation (4) with the observed flux F_ν(observed). Figure 1 shows the resulting histogram along with its best-fit Gaussian function. Since a Gaussian function is an excellent fit to the histogram in Figure 1, the extra error source is random rather than systematic. From the standard deviation of our model Gaussian, we find that the dispersion of N across our sample is $\Sigma = 1.93\sigma$. Accordingly, we increase our spectrophotometric error estimates by a factor of 1.93 to select only debris disks with 3Σ or greater excesses. The cross-hatching in Figure 1 demarcates the part of the N distribution where the debris disks lie. With the aforementioned detection procedure, we find

[7] See a description of these problems at http://ssc.spitzer.caltech.edu/irs/features.

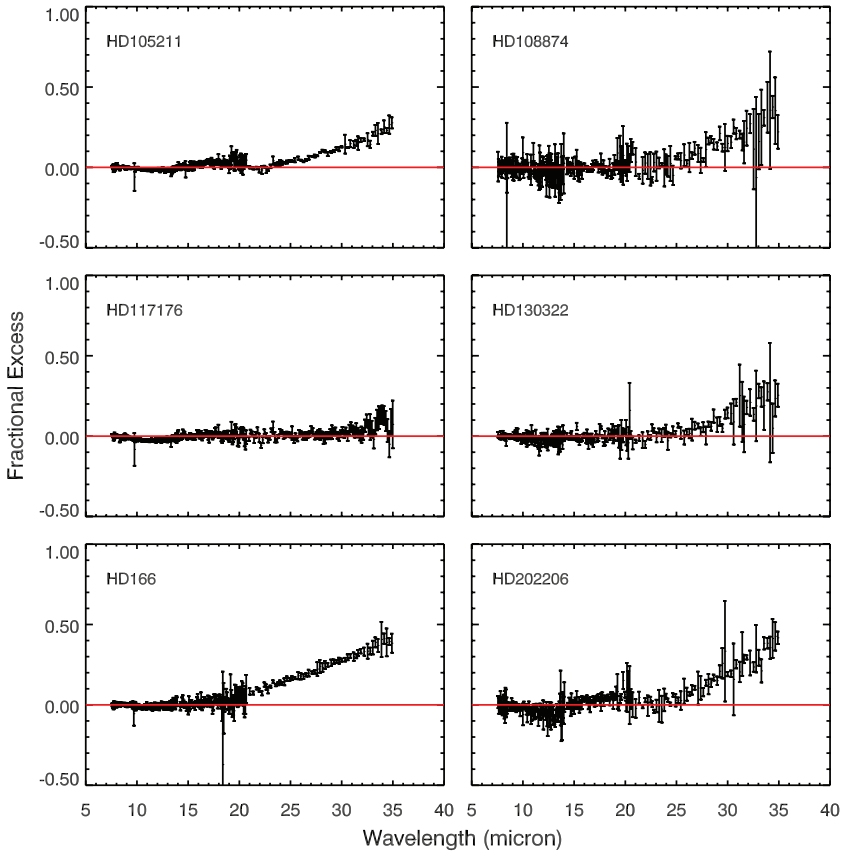

Figure 2. Debris disks in our sample have fractional excess spectra that rise toward longer IRS wavelengths. Only a few have any noticeable rise near 24 μm, consistent with the paucity of 24 μm excesses observed by the MIPS instrument. Several spectra show the well-known SL1 order droop. HD 108874, HD 117176, HD 130322, and HD 202206 are planet hosts.

(A color version of this figure is available in the online journal.)

statistically significant 32 μm excesses in the spectra of 11 stars. In the next section we discuss the spectra of our debris disks.

5. DEBRIS DISKS

Table 2 shows the results of our 30–34 μm spectrophotometry. The HD numbers of debris disks appear in bold in the table. We detect two new debris disks orbiting the planet hosts HD 108874 and HD 130322. We also measure 30–34 μm emission from nine other debris disks previously detected at 70 μm, four of which orbit planet hosts. The table also gives fractional dust fluxes at 30–34 μm and total luminosities for each star in the sample. Assuming the dust is a single-temperature blackbody, its luminosity is

$$\frac{L_{\rm dust}}{L_*} = \frac{F_{\rm dust}}{F_*} \frac{kT_{\rm dust}^4 \left(\exp\left[h\nu/kT_{\rm dust}\right] - 1\right)}{h\nu T_*^3}, \qquad (6)$$

where $F_{\rm dust} = F_{\rm obs} - F_*$. When the dust temperature is not known, one can use Equation (6) to calculate the minimum dust luminosity, assuming the emission peak of the dust is centered in the spectrophotometric filter. For peak dust luminosity at 32 μm, $T_{\rm dust} = 115$ K.

One can calculate the true luminosity ratio by detecting the debris disk at multiple wavelengths. We write Equation (6) once each for our 32 μm spectrophotometric fluxes and the MIPS 70 μm values from the literature and solve the resulting system for $T_{\rm dust}$ and $L_{\rm dust}/L_*$. Note that Equation (6) assumes that the dust has a single temperature—debris disks containing a large range of grain sizes or occupying a wide range of distances from the star will have a range of dust temperatures.

Table 2 contains three different types of measurements of $L_{\rm dust}/L_*$: true values, lower limits, and pseudo-upper limits. For stars without any measured infrared excess, we use Equation (6) and set $F_{\rm dust} = 3\Sigma$ to calculate the maximum dust luminosity assuming the excess emission comes from single-temperature dust at 115 K. For cold, faint dust undetected by both MIPS and IRS, the true luminosity may be higher than the maximum value we calculated if the dust emission peaks at very long wavelengths. Lower limits to the dust luminosity arise for debris disks with a detection at only one wavelength and true values come from detections at multiple wavelengths (see Section 6).

Figures 2 and 3 show the spectra of the debris disks in our sample. Each debris disk has little or no fractional infrared excess in the IRS SL1 and LL2 modules but a positive fractional excess slope in the long wavelengths of the LL1 module. Two of the debris disks, HD 219482 and HD 166, show strong evidence of 24 μm emission. For comparison, we also show the spectra of three stars without any significant infrared excess in Figure 4. These spectra tightly hug the line of zero fractional excess at all wavelengths and do not show a positive fractional excess slope in LL1. Note that the spectrum of HD 50499 shows the SL1 order curvature between 10 and 13 μm. As explained in Section 4, we chose the first ten unclipped resolution elements of LL1 (20.93–22.45 μm) to define our photosphere in order to avoid this order droop.

Our overall detection rate of debris disks is 11%, but the non-uniform sensitivity and the inclusion of 70 μm follow-up

Table 2
IRS 30–34 μm Spectrophotometric Results

HD	Name	F_* (mJy)	$F_{\rm obs}$ (mJy)	Σ	$F_{\rm dust}/F_*$	$\frac{L_{\rm dust}}{L_*} \times 10^5$[a]	$T_{\rm dust}$ (K)[b]
...	GJ 581	16.1	17.1	0.99	0.06	> 12	<83
...	GJ 876	24.8	25.3	0.67	0.02	< 5.5	
...	Hip 14810	7.5	7.0	0.93	−0.07	< 3.7	
142		30.9	30.8	2.67	0.00	> 3.0	<119
166		78.9	119	2.00	0.50	7.4	79 ± 3
1237	GJ 3021	39.9	38.7	1.71	−0.03	< 1.7	
3651		98.6	101.0	2.29	0.02	< 0.8	
4203		5.8	5.9	0.40	0.01	< 2.0	
4208		12.8	13.1	0.87	0.02	< 2.0	
8574		19.2	17.7	1.57	−0.08	< 1.9	
10697	109 Psc	48.7	48.1	1.98	−0.01	< 1.2	
11964		8.3	8.3	1.39	0.00	< 5.7	
12661		18.7	19.6	0.86	0.05	< 1.4	
13445	GJ 86	90.3	88.3	3.00	−0.02	< 1.3	
16141		32.4	31.4	1.72	−0.03	< 1.4	
17051	HR 810	107.4	108.9	2.34	0.01	< 0.5	
19994		126.0	124.0	2.91	−0.02	> 6.9	<83
20367		76.0	76.1	1.43	0.00	< 0.4	
20782		20.3	20.0	1.29	−0.02	< 1.7	
23079		20.1	21.0	1.11	0.05	< 1.3	
23127		5.5	4.9	0.65	−0.10	< 2.8	
23596		24.9	25.0	1.16	0.00	< 1.1	
27442	ϵ Ret	241.0	240.9	3.52	−0.30	< 0.4	
27894		2.5	2.5	0.67	−0.02	< 12	
28185		13.2	13.1	0.59	−0.01	< 1.3	
30177		8.4	8.0	0.51	−0.05	< 1.8	
33262	ζ Dor	177.3	192.9	1.64	0.09	0.8	91 ± 12
33283		8.5	9.5	0.81	0.12	< 2.2	
33564		109.6	112.3	2.78	0.03	< 0.5	
33636		24.4	29.7	0.85	0.22	5.2	61 ± 3
37124		16.4	14.9	1.18	−0.09	< 2.2	
37605		7.6	8.4	0.51	0.11	< 2.3	
40979		27.4	28.7	0.90	0.05	> 1.6	<67
41004	HD 41004 A	11.7	12.2	0.61	0.04	< 2.5	
45350		6.4	6.4	0.47	−0.01	< 2.2	
46375		10.7	11.5	6.66	0.07	> 3.2	<74
49674		10.3	10.6	0.40	0.03	< 1.2	
50499		18.1	18.3	0.65	0.01	> 1.8	<68
50554		25.6	31.0	0.68	0.21	6.2	58 ± 3
52265		41.0	44.5	0.66	0.09	2.9	56 ± 4
63454		7.1	7.3	0.47	0.03	< 3.5	
65216		11.4	10.1	0.63	−0.11	< 1.6	
68988		8.3	8.9	0.32	0.08	< 1.0	
70642		23.5	23.0	0.63	−0.02	< 0.8	
72659		16.5	17.7	0.67	0.08	< 1.0	
73256		12.3	11.8	0.52	−0.05	< 1.4	
74156		12.2	11.5	0.58	−0.06	< 1.1	
75289		38.1	31.7	1.54	−0.17	< 0.9	
76700		10.4	10.0	0.70	−0.05	< 2.0	
81040		16.0	16.5	0.84	0.03	< 1.6	
83443		10.8	9.5	0.41	−0.12	< 1.3	
88133		14.7	14.0	0.56	−0.05	< 1.3	
89307		25.5	25.0	0.84	−0.02	< 0.9	
89744		53.7	53.8	2.47	0.00	< 1.0	
93083		10.0	10.0	0.46	0.00	< 2.1	
99492		30.6	31.4	1.08	0.03	< 0.8	
102117		19.5	20.4	1.09	0.05	< 1.7	
102195		13.3	13.9	0.42	0.04	< 1.1	
105211	η Cru	178.5	215.6	3.30	0.21	6.7	51 ± 2
107148		10.4	9.6	0.68	−0.08	< 1.7	
108147		29.4	29.2	0.99	−0.01	< 0.8	
108874		5.9	7.9	0.33	0.32	> 1.2	$57 < T < 120$
109749		8.0	7.5	0.61	−0.06	< 1.8	
111232		54.4	54.3	1.26	0.00	< 0.7	
114386		12.5	13.7	0.71	0.09	< 3.0	
114762		19.3	19.7	1.13	0.02	< 1.5	

Table 2
(Continued)

HD	Name	F_* (mJy)	F_{obs} (mJy)	Σ	F_{dust}/F_*	$\frac{L_{dust}}{L_*} \times 10^5$[a]	T_{dust} (K)[b]
114783		21.1	20.7	1.39	−0.02	< 2.6	
117176	70 Vir	173.0	182.1	2.87	0.05	1.0	72 ± 10
117207		21.1	18.6	1.61	−0.12	< 2.3	
117618		21.2	20.4	1.04	−0.04	< 1.3	
130322		13.0	16.1	0.58	0.24	> 7.9	$61 < T < 120$
134987	23 Lib	39.9	40.4	0.76	0.01	< 0.5	
136118		26.7	26.3	0.88	−0.01	< 0.8	
142415		17.6	19.2	0.59	0.09	< 0.9	
143761	ρ Cr B	87.2	87.6	2.19	0.01	< 0.6	
145675	14 Her	53.2	50.7	2.57	−0.05	< 1.9	
147513		110.5	115.4	2.78	0.05	< 0.7	
149026		7.8	7.9	0.35	0.02	< 1.0	
149143		10.8	11.5	0.31	0.06	< 0.8	
154857		29.1	29.5	0.94	0.01	< 1.0	
159868		23.71	21.93	0.78	−0.075	< 0.6	
160691	μ Arae	247.1	247.3	2.36	0.00	< 0.3	
162020		10.2	9.5	0.36	−0.07	< 1.9	
168443		30.4	29.8	1.70	−0.02	< 1.7	
169830		50.2	51.3	1.31	0.02	< 0.5	
177830		43.4	42.4	2.48	−0.02	< 2.6	
183263		9.7	10.8	0.51	0.12	< 1.2	
185269		34.5	35.0	1.43	0.02	< 1.0	
186427	16 Cyg B	52.6	54.2	3.74	0.03	< 2.1	
187085		16.7	16.9	0.80	0.01	> 2.3	<67
187123		12.5	12.8	0.57	0.03	< 1.2	
188015		9.1	7.5	0.91	−0.18	< 3.0	
188753	HD 188753 A	24.6	24.3	1.17	−0.01	< 1.6	
190360		91.1	94.4	1.83	0.05	< 0.6	
192263		22.4	21.9	1.04	−0.02	> 5.1	<63
192699		84.0	85.6	2.48	0.02	< 1.2	
195019		31.2	32.7	0.80	0.03	< 0.8	
196050		14.9	16.4	1.52	0.10	< 2.7	
196885		25.9	1.00	0.00	< 0.9		
202206		10.4	14.3	0.35	0.38	12	57 ± 3
208487		13.5	12.3	0.69	−0.09	< 1.2	
210277		53.9	55.3	1.98	0.03	< 1.3	
212301		11.2	11.7	0.64	0.04	< 1.3	
213240		34.2	34.4	1.50	0.01	< 1.2	
216435		59.3	67.0	2.81	0.13	> 2.1	<70
216770		10.2	10.4	0.55	0.02	< 1.9	
217107		56.9	55.1	3.64	−0.03	< 1.9	
219482		66.5	91.0	1.15	0.37	3.7	81 ± 3[c]
222404	γ Cep	1622.0	1637.0	8.36	0.01	< 0.2	
222582		12.4	12.1	0.59	−0.03	< 1.3	
224693		6.3	6.1	0.62	−0.03	< 2.3	

Notes.
[a] Upper limits to the dust luminosity are calculated assuming a single-temperature blackbody with $T_{dust} = 115$ K. For cold dust undetected by both MIPS and IRS, the true luminosity ratio may be higher than the value quoted here. See Section 5 for further discussion of the relationship between observed 30–34 μm fluxes and grain luminosity.
[b] Grain temperature estimates are based on the blackbody approximation. For a discussion of temperature as a function of grain size, see Section 6.
[c] Our temperature measurement for the circumstellar dust of HD 219482 agrees with that of Beichman et al. (2006), who calculated $T_{dust} = 82 \pm 3$ K based on 24 and 70 μm photometry.

observations in our survey bias this statistic. Because of the non-uniformity of our observations, we do not attempt to calculate an error bar for our detection rate. However, our results agree with the IRS study of Beichman et al. (2006b), who found 32 μm excesses around $12\% \pm 5\%$ of stars in a sample that also included follow-ups of 70 μm excesses. Similarly, Lawler et al. (2009) report a 32 μm excess detection rate of $11.8\% \pm 2.4\%$.

The most intrinsically luminous debris disk in our sample is that orbiting the planet host HD 202206, which has $L_{dust}/L_* > 10^{-4}$. For comparison, the well-studied debris disks orbiting the planet hosts HD 69830 and HD 82943 have luminosity ratios L_{dust}/L_* of 2×10^{-4} and 1.2×10^{-4}, respectively (Beichman et al. 2005). All but two of the 111 stars in our sample have a minimum 3Σ detectability of $L_{dust}/L_* < 10^{-4}$; thus only $\sim$1% of the sample has a fractional dust luminosity brighter than $10^{-4} L_*$. Our result agrees with the $2\% \pm 2\%$ detection rate for excesses of $L_{dust}/L_* > 10^{-4}$ calculated by Bryden et al. (2006).

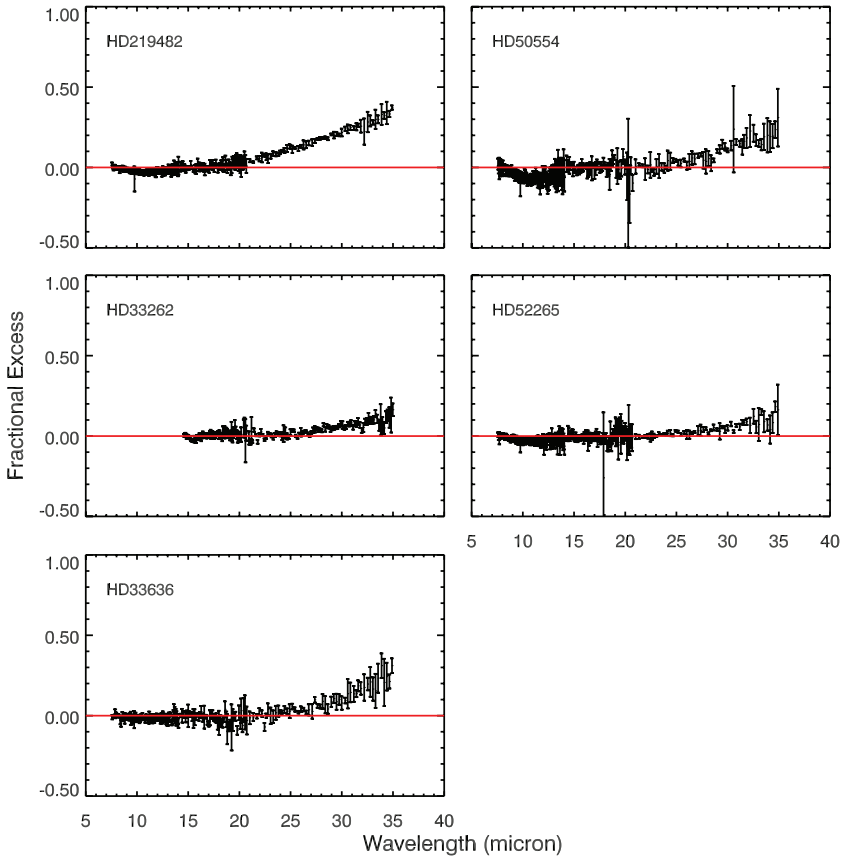

Figure 3. Fractional excess spectra of detected debris disks, continued. No SL data points are included for HD 33262 because the SL1 spectra were partially saturated. HD 50554 and HD 52265 are planet hosts.

(A color version of this figure is available in the online journal.)

6. DUST TEMPERATURE AND LOCATION

We will now determine the location of the debris for the sample of 11 stars with infrared excesses detected at 32 μm. Of our 11 detected debris disks, 9 also have excess emission at 70 μm (Beichman et al. 2006a; Trilling et al. 2008; Bryden et al. 2009; Kóspál et al. 2009). Table 2 lists the blackbody temperature of each debris disk detected at multiple wavelengths. Beichman et al. (2006a) detected HD 219482's dust at both 24 and 70 μm and calculated $T_{\rm dust} = 82 \pm 3$ K for large grains, in excellent agreement with our value of 81 ± 3 K. Our 79 ± 3 K temperature for the dust orbiting HD 166 does not agree with Tanner et al. (2009), who calculated a lower limit of 104 K using the previously published 70 μm detection (Trilling et al. 2008) and the 160 μm upper limit. However, grain temperature varies with size roughly as

$$T_{\rm dust} = 4.0 \left(\frac{L_*}{r_{\rm gr}} \right)^{1/6} a^{-1/3}, \quad (7)$$

where $r_{\rm gr}$ is the grain radius and a is the semimajor axis of the debris orbit (Kruegel 2003). Therefore each photometric band is most sensitive to a certain combination of grain size and distance from the star. Different pairs of photometric bands may lead to different grain temperature distance estimates (Carpenter et al. 2009).

By combining our IRS observations with previous MIPS data, we have obtained temperature estimates for 15 planet hosts and 5 non-host stars. Figure 5 shows luminosity ratio versus dust temperature for all debris disks in our sample, whether detected in this study or previous 70 μm MIPS work. The warmest temperature of a debris disk detected at multiple wavelengths is 91 K for the dust around HD 33262. Only four stars may possibly host dust warmer than 100 K—HD 142, HD 33262, HD 108874, and HD 130322 have temperature upper limits of 117 K, 103 K, 120 K, and 120 K, respectively. Our finding that debris disks around solar-type stars are primarily cold agrees with Hillenbrand et al. (2008), who find dust temperatures <45–85 K for the 25 debris disks in the FEPS Spitzer Legacy Science Program. 70 μm debris systems with temperature upper limits only may be true Kuiper Belt analogs, as most have $T_{\rm dust} < 70$ K.

With the exception of three of the upper limits quoted above, all dust temperatures are below the water–ice sublimation temperature of $T \sim 110$ K in a zero-pressure medium. However, in optically thin disks photodesorption is the dominant volatile removal mechanism and is efficient well beyond the thermal ice line (Grigorieva et al. 2007). Indeed, the survival timescale for ice deposited in monolayers on the surfaces of small grains in an optically thin disk is of order a few minutes (Chen et al. 2005). Assuming, accordingly, that (1) the dust in each system is rocky or carbonaceous with an albedo near zero and (2) most grains are larger than 10 μm and so have absorption coefficients $Q \sim 1$ for visible and near-IR irradiation, we can find the distance of the dust from its host star in the blackbody approximation, appropriate for large grains:

$$a = \frac{R_*}{2} \frac{T_*^2}{T_{\rm dust}^2}, \quad (8)$$

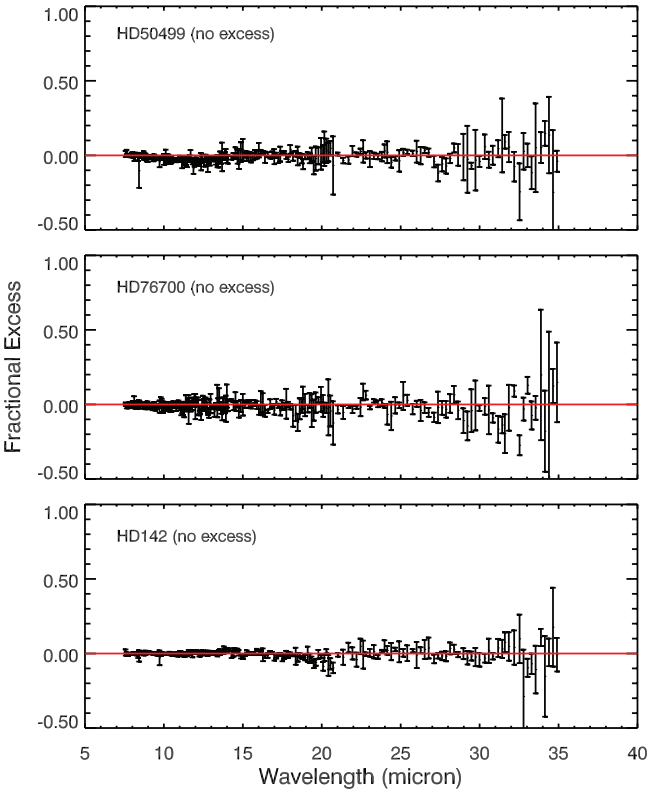

Figure 4. Fractional excess spectra of stars with no significant 30–34 μm emission. These stars show no noticeable rise in excess toward long wavelengths.

where R_* is the star radius. For our solar-type stars with $60 \lesssim T_{\rm dust} \lesssim 100$ K, we find 7 AU $\lesssim a \lesssim$ 20 AU. Large grains in the debris disks we have discovered at 32 μm occupy what would be the region between Saturn and Uranus in our own solar system.

Smaller grains in the 60–100 K temperature range would reside on larger orbits. We estimate the minimum grain size in our debris disks from the radiation pressure blowout limit (Artymowicz 1988) of

$$r_{\rm min} = \frac{3 L_* Q_{\rm pr}}{16 \pi G M_* c \rho}, \quad (9)$$

where $r_{\rm min}$ is the minimum grain size, L_* and M_* are the star luminosity and mass, $Q_{\rm pr}$ is the radiation pressure coupling coefficient, and ρ is the internal density of the grains. $Q_{\rm pr} = 1$ is a good approximation for solar-type stars (Kruegel 2003). For silicate grains with $\rho = 3.3$ g cm^{-3}, $a_{\rm min} = 0.1$ μm. Icy grains with $\rho = 1.0$ g cm^{-3} orbiting a solar-type star have minimum size $a_{\rm min} = 0.3$ μm. Using Equation (7), which applies to grain sizes from approximately 0.03 to 30 μm (Kruegel 2003), we find that 70 K silicate grains at the blowout limit orbit ~240 AU from solar-type stars. Low-density icy grains, which would be destroyed quickly by photodesorption, are limited to within ~142 AU from their host stars.

In the introduction, we emphasized the lack of any dynamical connection between short-period planets and cold dust—planets detected by radial velocity neither migrated through and destroyed our planetesimal belts, nor dynamically stir them today. Based on the 240 AU maximum orbital radius of grains with temperatures near 70 K, a representative temperature for our detected debris disks, we can restrict the formation locations of the known radial-velocity planets to within ~240 AU.

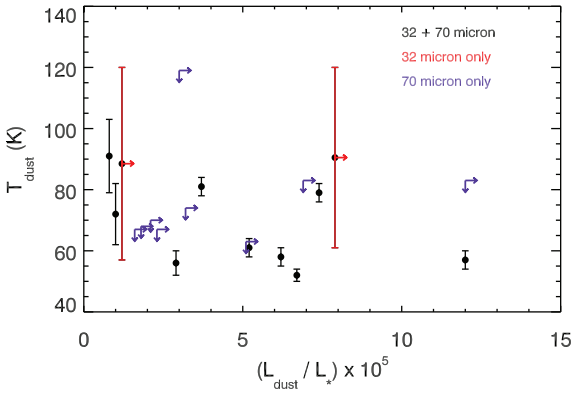

Figure 5. Dust luminosity vs. temperature for all debris disks in our sample. Black circles indicate the debris disks detected at both 32 and 70 μm. Red error bars indicate the possible temperature range for debris disks detected only at 32 μm while right-pointing red arrows denote that the luminosity ratios for these debris disks are lower limits only. Purple points with double arrows denote the debris disks detected only at 70 μm, which gives upper limits for temperatures and lower limits for luminosities. Only four stars, HD 142, HD 33262, HD 108874, and HD 130322, may have debris rings with dust hotter than 100 K (see Section 6).

In any individual debris system where the bulk of the infrared excess emission comes from large, near-blackbody grains, we can restrict the giant planet formation zone even further, excluding regions beyond 15 AU. In such systems, giant planet formation by core accretion would have been restricted to a narrow belt near the ice line, consistent with the theoretical predictions of Dodson-Robinson et al. (2009b). So far, the orbital radii of the 15 debris disks orbiting planet hosts in this sample provide the only purely observational constraint on where the radial-velocity planets could have formed.

7. CONCLUSIONS

We searched a sample of 111 stars, including 105 planet hosts, for 30–34 μm excess emission indicating circumstellar dust. Out of 111 stars, 11 showed detectable 32 μm spectrophotometric excess. Our debris disk detection rate of 11% is consistent with previous IRS and MIPS 70 μm studies of solar-type stars. We have identified two new debris disks orbiting HD 108874 and HD 130322 and calculated dust temperatures and luminosities for the debris disks that had been previously detected at 70 μm.

Our IRS data show that the majority of debris systems contain cold dust with $T_{\rm dust} < 100$ K. Here we confirm earlier results from 24 μm photometry (Bryden et al. 2006) and IRS spectroscopy (Hillenbrand et al. 2008) demonstrating that excess emission is usually detectable only at wavelengths longer than 30 μm. The exception in our survey that has noticeable excess at 20 μm, HD 166, is cooler than 80 K. Lower limits to the circumstellar dust temperatures of solar-type stars come from the MIPS 160 μm photometry of Tanner et al. (2009); they find that $T_{\rm dust} > 27$ K for the majority of the debris disks in their sample. While all of our debris disks are colder than the ice sublimation temperature, we expect them to contain mainly bare rock/carbonaceous grains since photoevaporation of ice is extremely efficient in optically thin disks (Grigorieva et al. 2007).

The cold temperatures of most circumstellar dust disks make them excellent candidates for follow-up with the *Herschel Space Observatory* (Pilbratt et al. 2010). The PACS medium-resolution spectrometer, which covers 55–210 μm at a resolution of $R = \lambda/\Delta\lambda = 1000$–4000 and also includes photometric bands, will cover the peak blackbody emission of such disks and

provide detailed dust spectral energy distributions (SEDs). Circumstellar dust SEDs constrain the location of the emitting dust and show whether it occupies a narrow ring—the simplifying assumption used in this work—or a broad, multi-AU band (e.g., Hillenbrand et al. 2008). If any debris disks contain icy dust produced by very recent collisions, PACS may be able to detect H_2O gas produced by photoevaporation of the grain mantles.

One question open for debate is why the planetesimal belts surrounding our host stars did not accumulate into giant planets. While planets may shape debris disk edges (Quillen 2006), they will eject planetesimals within a few Roche lobe radii of their orbits (Bryden et al. 2000), so planets and circumstellar dust should not coincide. Planet-formation simulations show that formation of ice giants such as Uranus and Neptune is robust out to ∼15 AU in disks of several times the minimum-mass solar nebula (Dodson-Robinson et al. 2009a; Dodson-Robinson & Bodenheimer 2010). Blackbody grains with $T_{\rm dust} = 70$ K reside only 15 AU from solar-type stars.

If most of our debris disk luminosity comes from blackbody grains, a simple explanation for the presence of planetesimal belts in locations that could theoretically host planets is that the majority of protostellar disks do not have enough mass to form ice giants near ∼15 AU. Gas and ice giant formation by core accretion would then be restricted to a narrow region around the ice line in most disks, as predicted by Dodson-Robinson et al. (2009b). The Sun's ability to form Uranus and Neptune in the trans-Saturnian region (Dodson-Robinson & Bodenheimer 2010) would be the unusual result of an abnormally massive solar nebula.

If most of the infrared excess emission is produced by small grains near the radiation-pressure blowout limit, we can in general confine the ensemble of radial-velocity planets to formation zones less than 240 AU from host stars. We have therefore presented the first fully observational constraints on the formation locations of the ensemble of radial-velocity planets.

Support for S.D.R.'s work at NASA Exoplanet Science Institute was provided by NASA through the Spitzer Space Telescope Fellowship Program. S.D.R.'s work at University of Texas was supported by the Dean's Fellowship program of UT's College of Natural Sciences. J.C. was partially supported by a contract from JPL/Caltech. S.D.R. acknowledges input on IRS data reduction from Joel Green. This research has made use of the following online resources: the SIMBAD database, VizieR catalogue access tool, and Aladin sky atlas operated at CDS, Strasbourg, France; the NASA/IPAC/NExScI Star and Exoplanet Database and the NASA/IPAC Infrared Science Archive, which are operated by the Jet Propulsion Laboratory, California Institute of Technology, under contract with the National Aeronautics and Space Administration; and the Extrasolar Planets Encyclopaedia at http://exoplanet.eu.

REFERENCES

Artymowicz, P. 1988, ApJ, 335, L79
Aumann, H. H., et al. 1984, ApJ, 278, L23
Beichman, C. A., et al. 2005, ApJ, 622, 1160
Beichman, C. A., et al. 2006a, ApJ, 652, 1674
Beichman, C. A., et al. 2006b, ApJ, 639, 1166
Bertone, E., Buzzoni, A., Chávez, M., & Rodríguez-Merino, L. H. 2004, AJ, 128, 829
Bessell, M. S. 1990, A&AS, 83, 357
Bessell, M. S. 1995, PASP, 107, 672
Bodenheimer, P., Hubickyj, O., & Lissauer, J. J. 2000, Icarus, 143, 2
Bryden, G., Lin, D. N. C., & Ida, S. 2000, ApJ, 544, 481
Bryden, G., et al. 2006, ApJ, 636, 1098
Bryden, G., et al. 2009, ApJ, 705, 1226
Butler, R. P., et al. 2006, ApJ, 646, 505
Carpenter, J. M., Mamajek, E. E., Hillenbrand, L. A., & Meyer, M. R. 2009, ApJ, 705, 1646
Chen, C. H., et al. 2005, ApJ, 634, 1372
Chen, C. H., et al. 2006, ApJS, 166, 351
Cochran, W. D., et al. 2004, ApJ, 611, L133
Cutri, R. M., et al. 2003, The IRSA 2MASS All-Sky Point Source Catalog, NASA/IPAC Infrared Science Archive, http://irsa.ipac.caltech.edu/applications/Gator/
da Silva, R., et al. 2006, A&A, 446, 717
Dodson-Robinson, S. E., & Bodenheimer, P. 2010, Icarus, 207, 491
Dodson-Robinson, S. E., Veras, D., Ford, E. B., & Beichman, C. A. 2009a, ApJ, 707, 79
Dodson-Robinson, S. E., Willacy, K., Bodenheimer, P., Turner, N. J., & Beichman, C. A. 2009b, Icarus, 200, 672
Eggenberger, A., Udry, S., Mazeh, T., Segal, Y., & Mayor, M. 2007, A&A, 466, 1179
Fischer, D. A., et al. 2005, ApJ, 620, 481
Fischer, D. A., et al. 2006, ApJ, 637, 1094
Flower, P. 1996, ApJ, 469, 355
Goldreich, P., Lithwick, Y., & Sari, R. 2004, ApJ, 614, 497
Gomes, R., Levison, H. F., Tsiganis, K., & Morbidelli, A. 2005, Nature, 435, 466
Grigorieva, A., Thébault, Ph., Artymowicz, A., & Brandeker, A. 2007, A&A, 475, 775
Hauschildt, P. H., Allard, F., & Baron, E. 1999, ApJ, 512, 377
Higdon, S. J. U., et al. 2004, PASP, 116, 975
Hillenbrand, L. A., et al. 2008, ApJ, 677, 630
Høg, E., et al. 2000, A&A, 355, L27
Ida, S., & Lin, D. N. C. 2004, ApJ, 604, 388
Johnson, J. A., et al. 2006, ApJ, 647, 600
Johnson, J. A., et al. 2007, ApJ, 665, 785
Kalas, P., et al. 2008, Science, 322, 1345
Konacki, M. 2005, Nature, 436, 230
Kóspál, Á., Ardila, D. R., Moór, A., & Ábrahám, P. 2009, ApJ, 700, L73
Kruegel, E. 2003, The Physics of Interstellar Dust (IoP Series in Astronomy and Astrophysics; Bristol: Institute of Physics Publishing)
Kurucz, R. L. 1992, in IAU Symp. 149, The Stellar Populations of Galaxies, ed. B. Barbuy & A. Renzini (Dordrecht: Kluwer), 225
Lawler, S. M., et al. 2009, ApJ, 705, L89
Libert, A.-S., & Tsiganis, K. 2009, A&A, 493, 677
Lin, D. N. C., Bodenheimer, P., & Richardson, D. C. 1996, Nature, 380, 606
Lo Curto, G., et al. 2006, A&A, 451, 345
Lovis, C., et al. 2005, A&A, 437, 1111
Lovis, C., et al. 2006, Nature, 441, 305
Mayor, M., Udry, S., Naef, D., Pepe, F., Queloz, D., Santos, N. C., & Burnet, M. 2004, A&A, 415, 391
Melo, C., et al. 2007, A&A, 467, 721
Moro-Martín, A., et al. 2007, ApJ, 658, 1312
Nordström, B., et al. 2004, A&A, 418, 989
Peletier, R. F. 1989, PhD thesis, Univ. of Groningen, The Netherlands
Perryman, M. A. C., et al. 1997, A&A, 323, L49
Pilbratt, G. L., et al. 2010, A&A, 518, L1
Quillen, A. 2006, MNRAS, 372, L14
Raymond, S. N., Mandell, A. M., & Sigurdsson, S. 2006, Science, 313, 1413
Rocha-Pinto, H. J., & Maciel, W. J. 1998, MNRAS, 298, 332
Saffe, C., Gómez, M., & Chavero, C. 2005, A&A, 443, 609
Santos, N. C., Israelian, G., & Mayor, M. 2004a, A&A, 415, 1153
Santos, N. C., Israelian, G., Mayor, M., Bento, J. P., Almeida, P. C., Sousa, S. G., & Ecuvillon, A. 2005, A&A, 437, 1127
Santos, N. C., Israelian, G., Mayor, M., Rebolo, R., & Udry, S. 2003, A&A, 398, 363
Santos, N. C., et al. 2002, A&A, 392, 215
Santos, N. C., et al. 2004b, A&A, 426, L19
Sato, B., et al. 2005, ApJ, 633, 465
Sozzetti, A., et al. 2006, A&A, 449, 417
Su, K. Y. L., et al. 2006, ApJ, 653, 675
Tanner, A., Beichman, C., Bryden, G., Lisse, C., & Lawler, S. 2009, ApJ, 704, 109
Thommes, E. W., Duncan, M. J., & Levison, H. F. 2003, Icarus, 161, 431
Trilling, D. E., et al. 2008, ApJ, 674, 1086
Udry, S., et al. 2003, A&A, 407, 679
Valenti, J. A., & Fischer, D. A. 2005, ApJS, 159, 141 (VF05)
Wright, J. T., Marcy, G. W., Butler, R. P., & Vogt, S. S. 2004, ApJS, 152, 261
Wright, J. T., et al. 2009, ApJ, 699, L97